ARTICLE OPEN

Check for updates

Spin-orbit coupled spin-polarised hole gas at the $CrSe_2$-terminated surface of $AgCrSe_2$

Gesa-R. Siemann[1], Seo-Jin Kim[2], Edgar Abarca Morales[1,2], Philip A. E. Murgatroyd[1], Andela Zivanovic[1,2], Brendan Edwards[1], Igor Marković[1,2], Federico Mazzola[1], Liam Trzaska[1], Oliver J. Clark[1], Chiara Bigi[1], Haijing Zhang[2], Barat Achinuq[3], Thorsten Hesjedal[3,4], Matthew D. Watson[4], Timur K. Kim[4], Peter Bencok[4], Gerrit van der Laan[4], Craig M. Polley[5], Mats Leandersson[5], Hanna Fedderwitz[5], Khadiza Ali[5,6], Balasubramanian Thiagarajan[5], Marcus Schmidt[2], Michael Baenitz[2], Helge Rosner[2] and Phil D. C. King[1]✉

In half-metallic systems, electronic conduction is mediated by a single spin species, offering enormous potential for spintronic devices. Here, using microscopic-area angle-resolved photoemission, we show that a spin-polarised two-dimensional hole gas is naturally realised in the polar magnetic semiconductor $AgCrSe_2$ by an intrinsic self-doping at its $CrSe_2$-terminated surface. Through comparison with first-principles calculations, we unveil a striking role of spin-orbit coupling for the surface hole gas, unlocked by both bulk and surface inversion symmetry breaking, suggesting routes for stabilising complex magnetic textures in the surface layer of $AgCrSe_2$.

npj Quantum Materials (2023)8:61 ; https://doi.org/10.1038/s41535-023-00593-4

INTRODUCTION

The layered compound $AgCrSe_2$ has attracted significant interest as a superionic conductor and a promising thermoelectric[1–5]. Its crystal structure (Fig. 1a) is comprised of layers of edge-sharing Cr-Se octahedra, separated by quasi-two-dimensional puckered honeycomb Ag layers. This is closely related to the delafossite crystal structure, in which most compounds crystalise in a rhombohedral structure that belongs to the centrosymmetric space group $R\bar{3}m$[6,7]. Unlike the delafossites, however, the Ag ions in $AgCrSe_2$ occupy only one of two triangular sublattices at low temperatures, leading to a non-centrosymmetric $R3m$ structure. With increasing temperature, Ag ions migrate to the second site until an order-disorder transition to a centrosymmetric $R\bar{3}m$ structure occurs at around 450 K, with equal population of both Ag sublattices[3,8,9] and a marked increase in superionic conduction[10].

As well as their role in ionic conduction, the Ag ions play a crucial role in the electronic structure of the $CrSe_2$ layers, stabilising Cr within a favourable Cr^{3+} formal oxidation state. These nominally $S = 3/2$ Cr ions order magnetically below $T_N = 32$ K. They carry an effective magnetic moment of $\approx 3.5\ \mu_B/Cr$[11–13], and form a long-period cycloidal magnetic structure within the Cr plane, with antiferromagnetic interlayer coupling[13,14]. Moreover, the Cr ions are thought to exhibit significant hybridisation with the ligand states[13,15], potentially unlocking pronounced spin-orbit coupling (SOC) effects which - in conjunction with the lack of bulk inversion symmetry - are likely key to understanding the complex magnetic textures in this system.

It is particularly interesting to consider modifications to the electronic structure of this system in the vicinity of its surface. Bulk-like terminations would lead to two natural surface types—a $CrSe_2$-terminated and Ag-terminated surface—which are both polar. In the bulk, the Cr^{3+} valence can be considered to result from charge transfer of, on average, half an electron per Ag ion into the $CrSe_2$ layer above the Ag plane, and half an electron per Ag ion into the $CrSe_2$ layer below, leaving the Ag in a nominal Ag^{1+} oxidation state (Fig. 1b). Such charge transfer processes will be suppressed at the surface, due to the missing bonding partner. The resulting $CrSe_2$ and Ag-terminated surfaces would thus be expected to be significantly hole- or electron-doped, respectively, relative to the bulk charge count. Such electronic reconstructions were found to significantly modify the electronic structure in the vicinity of the surface for the sister family of delafossite oxides[16,17]. In particular, at the CoO_2-terminated surface of $PtCoO_2$, a set of surface states are formed that host a large Rashba-type spin splitting, mediated by giant inversion symmetry breaking at the surface[16]. It is of significant interest to explore such effects at the $CrSe_2$-terminated surface of $AgCrSe_2$, to investigate the resulting interplay between the bulk and surface inversion symmetry breaking, SOC, and magnetism in this system. We study this here, employing microscopic-area angle-resolved photoemission (ARPES, see Methods) to directly probe the surface termination-dependent electronic structure of $AgCrSe_2$.

RESULTS

Termination-dependent electronic structure

Figure 1c–f shows the results of our spatially resolved photoemission measurements of the Se 3*d* and Ag 4*p* core levels. The Se 3*d* core levels (Fig. 1e) show a multi-peak structure, beyond the simple doublet expected from SOC, and which varies strongly for different regions of the sample (see sample locations from which these core level spectra were extracted in Fig. 1c). This points to the presence of different local electronic environments of the emitting atoms, as would naturally be expected for a cleaved surface of $AgCrSe_2$, where Ag- and $CrSe_2$-terminated regions would be expected to be distributed across the sample surface (we note that, in principle, separate core level components could

[1]SUPA, School of Physics and Astronomy, University of St Andrews, St Andrews, UK. [2]Max Planck Institute for Chemical Physics of Solids, Dresden, Germany. [3]Department of Physics, Clarendon Laboratory, University of Oxford, Oxford, UK. [4]Diamond Light Source, Harwell Science and Innovation Campus, Didcot, UK. [5]MAX IV Laboratory, Lund University, Lund, Sweden. [6]Department of Microtechnology and Nanoscience, Chalmers University of Technology, Göteborg, Sweden. ✉email: pdk6@st-andrews.ac.uk

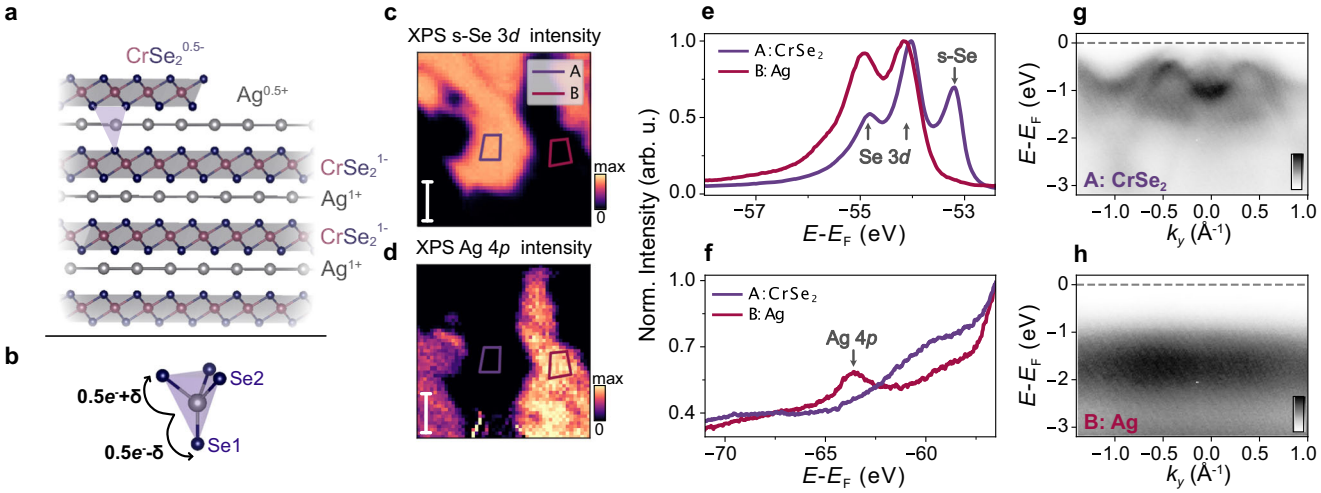

Fig. 1 Termination-dependent electronic structure of $AgCrSe_2$. **a** Crystal structure of $AgCrSe_2$, composed of alternating $CrSe_2^{1-}$ and Ag^{1+} layers, with the charge count set by interlayer charge transfer **b**. At the surface, the loss of bonding partners would be expected to result in an approximately $0.5h^+$ hole-doping ($0.5e^-$ electron-doping) of the $CrSe_2$ (Ag) terminated surface with respect to the bulk. **c**, **d** Both terminations would be expected for a typical cleaved surface, and are evident here from X-ray photoemission (XPS) spatial mapping. Marked spatial-dependent variations in **c** the intensity of a surface component of the Se 3*d* core level (s-Se) are anti-correlated with **d** the intensity of the Ag 4*p* core level with the scale corresponding to 25 μm for both maps. **e**, **f** Normalised **e** Se 3*d* and **f** Ag 4*p* XPS spectra extracted from the purple (A) and red (B) spatial regions in (c, d), representing $CrSe_2$- and Ag-terminated surfaces, respectively. **g**, **h** Corresponding ARPES spectra obtained from the same two areas, measured using a photon energy of 75 eV and linear-horizontal (LH) polarised light. All data has been taken at $T \approx 35$ K, i.e., above the magnetic transition temperature of $T_N = 32$ K.

be expected for the distinct Se1 and Se2 atomic species in the bulk. This splitting, however, would be expected to be small, and we do not resolve such a splitting here). We attribute, in particular, the low-energy feature of the Se 3*d* core level spectra at a binding energy of ≈ 53 eV as arising from Se states in a surface $CrSe_2$ layer (Fig. 1e, S-Se), where the surface core level shift is a consequence of the suppressed charge transfer into the $CrSe_2$ surface layer due to the missing Ag atoms that were previously above the surface plane[18,19]. The observation of such a shift here thus gives the first experimental evidence for hole doping as a result of an electronic reconstruction at the Se-terminated surface of $AgCrSe_2$.

Fitting the XPS data at each point of the spatial map we can track the amplitude of the low binding energy peak. We find a clear spatial variation on length scales of 25–50 μm, with an intensity variation which is anti-correlated with the amplitude of a Ag 4*p* core level peak (Fig. 1d, f). This confirms our assignment of the presence of a low-energy Se 3*d* component as a signature of the $CrSe_2$-terminated surface, while the regions of the sample lacking this component can be assigned as Ag-terminated surface regions. For the Ag-terminated surfaces, some relative variation in spectral weight of the Ag and Se core levels is evident (see also Supplementary Fig. 1). This likely reflects some local variation in the level of Ag-site disorder and its fractional surface coverage, although we find no evidence for either ordered atomic reconstructions or strongly mixed surface terminations. We thus group our surface terminations into $CrSe_2$ and Ag-terminated patches, respectively. With this identification, we can perform ARPES measurements of the valence band electronic structure from such regions, to probe their distinct surface-dependent electronic structures. Fig. 1(g, h) shows our measured ARPES spectra, extracted from spatial mapping data (see Supplementary Fig. 2) and integrated over the same regions as indicated in Fig. 1c, d for the core level spectra. For the Ag-terminated surface (Fig. 1h), we observe only diffuse spectral weight, peaking at a binding energy of ≈ 1.5 eV. This is in agreement with the location of a pronounced peak in the Cr partial density of states found in resonant photoemission measurements of $AgCrSe_2$[13], and we thus attribute this spectral weight to bulk-like Cr-derived states from the subsurface layers (see also Supplementary Fig. 3). The lack of any dispersive states for this surface likely results from high levels of Ag disorder, consistent with the relative spectral weight variations in core-level spectra discussed above. Indeed, even in the bulk, a small Ag off-stoichiometry has been reported[20], with additional site disorder persisting to low temperatures[13]. The disorder is likely higher at the cleaved Ag-surface, leading to significant scattering and thus only broad features being observed experimentally. In contrast, however, we observe clear dispersive states for the $CrSe_2$-terminated surface (Fig. 1g). We focus on these states for the remainder of the paper, and show detailed measurements of these in Fig. 2.

$AgCrSe_2$ is a *p*-type degenerate semiconductor, with bulk carrier densities on the order of 8×10^{19} cm^{-3}[15]. This should give rise to only small Fermi pockets, with a Fermi wavevector, $k_F \sim 0.1$ Å^{-1}. In contrast, our ARPES measurements (Fig. 2a, b) reveal two bands crossing the Fermi level along the Γ-K direction (blue and green arrows) which have large k_F values of 0.55 ± 0.02 Å^{-1} and 0.33 ± 0.02 Å^{-1}, respectively, indicating a well-defined metallic state. Similar features have been observed in a previous ARPES study[21] and were assigned to be part of the bulk band manifold. The associated carrier density, however, appears far too high to derive from the bulk states, even with plausible levels of off-stoichiometry[2,15,22]. Combined with the strong spatial variation in the measured electronic structure observed here, we thus instead attribute these metallic states as the result of a significant additional hole doping at the $CrSe_2$-terminated surface, resulting from its polar surface charge and consistent with the core level shifts discussed above. This leads to a distinct set of states, energetically split off from the bulk manifold and spatially localised at the surface. Consistent with this, our photon energy-dependent ARPES measurements (Fig. 2d) indicate that these states are non-dispersive with the out-of-plane momentum across multiple Brillouin zones in k_z. This indicates a completely two-dimensional character, confirming their surface-localised nature. We show in Fig. 2e our ARPES measurements of the resulting Fermi surfaces. Spectral weight at the Brillouin zone centre results from the top of the strongly dispersive hole states evident in Fig. 2b. These, however, do not cross the Fermi level, with the spectral weight present at E_F only due to finite broadening in the

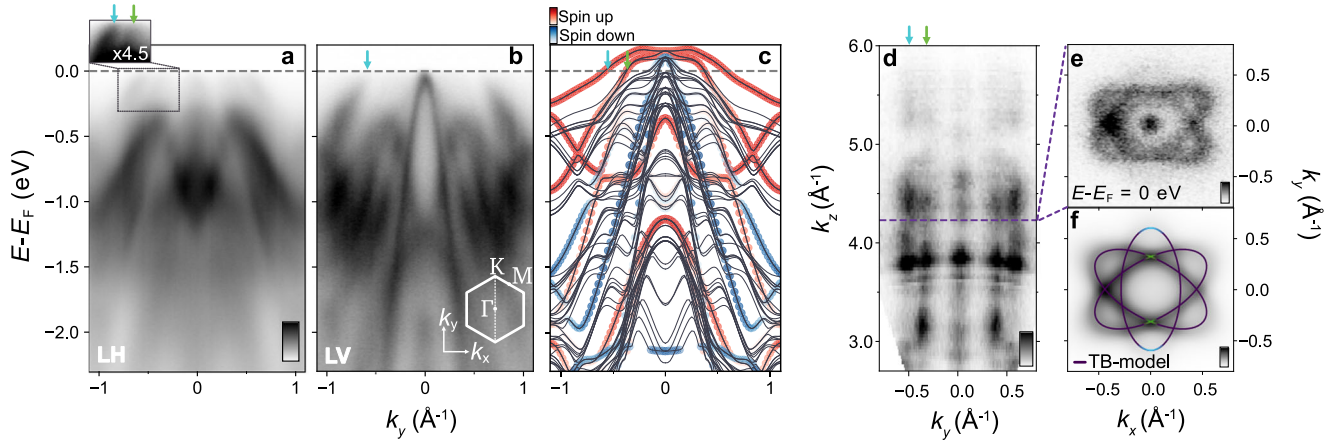

Fig. 2 Electronic structure of the $CrSe_2$-terminated surface. a, **b** ARPES data from the $CrSe_2$-terminated surface measured along the $\Gamma - K$ direction using $h\nu = 75$ eV and **a** linear horizontal (LH) and **b** linear vertical (LV) polarised light both measured at a temperature of $T \approx 18$ K below the magnetic transition of $T_N = 32$ K. Two bands can be observed crossing the Fermi level, indicated by the blue and green arrows. The inset in **a** shows the region indicated with enhanced contrast. **c** DFT calculations of a $CrSe_2$-terminated supercell, projected onto the spin-up and spin-down character of the top $CrSe_2$ layer. **d** Photon energy-dependent ARPES measurements ($h\nu = 20 - 140$ eV, LH polarised light, $T \approx 18$ K), allowing probing the momentum distribution curve at the Fermi level over multiple Brillouin zones in k_z. **e** Measured Fermi surface (LH polarised light, $T \approx 8$ K) in the $k_x - k_y$ plane, at the k_z value indicated by the dashed line in **d**, and **f** corresponding three-band minimal tight-binding model.

experimental spectra (see Supplementary Fig. 4)). The surface states discussed above, however, contribute largely hole-like Fermi surfaces.

Spin-polarised surface hole gas

Albeit exhibiting strong matrix element variations in our measurements, these Fermi surfaces are well described by three intersecting elliptical pockets (Fig. 2f). From the areas of these ellipses, we are able to directly determine the surface carrier density using Luttinger's theorem. If we assume that the observed electronic states are spin-degenerate, this would result in an unphysically high hole density of 1 ± 0.2 holes/surface Cr. If, on the other hand, we consider these states to be spin-polarised (i.e. singly degenerate) states, we obtain a surface doping of 0.5 ± 0.1 holes/Cr, which is in excellent agreement with the simple considerations for interlayer charge transfer introduced above[16,23–25], and well in line with the situation in the similar delafossite-type materials[16,17,26].

We thus attribute the Fermi surfaces observed here as arising from a high-density 2D hole gas of spin-polarised carriers, which naturally forms at the $CrSe_2$-terminated surface of $AgCrSe_2$ due to the intrinsic self-doping of this polar surface. To confirm this, we have performed density-functional theory (DFT) supercell calculations of the surface electronic structure of such a $CrSe_2$-terminated surface (see Methods). We show in Fig. 2c the electronic structure predicted by such calculations where we neglect SOC. Consistent with our experimental measurements, we find a complex multi-band electronic structure throughout the valence bands. Of core importance here, however, are the near-E_F states, which we show projected onto the surface $CrSe_2$ layer with spin-up (red) and spin-down (blue) characters. From this, we can identify the Fermi surfaces observed experimentally as arising exclusively from the spin-up carriers. Although spin-down states are seen to cross the Fermi level in the calculations, the top of the dispersive hole band visible in Fig. 2b is in reality located just below the Fermi level (see Supplementary Fig. 4). This discrepancy likely arises due to the slight off-stoichiometry inherent to the slab geometry of a material with polar surfaces. Experimentally, the location of this band just below the Fermi level establishes the surface hole gas here as a half-metal, comprised of just one species of spin-polarised carriers. Excitingly, however, the spin-majority states are located close by in energy, and so tuning of the Fermi level—for example using the field-effect—could be used to deliberately yield carriers of opposite spin orientation, leading to a tuneable spin polarisation of the surface layer.

In fact, we can already see small changes in the level of surface charge transfer for different samples studied here, shown in Fig. 3a, b. As well as significant variations in transition matrix elements, leading to a different intensity distribution across the measured bands, we find that k_F of the Fermi surfaces discussed above (blue and green arrows) are each increased by about 0.1 Å^{-1} in Fig. 3b as compared to Fig. 3a. Moreover, dispersive hole bands additionally appear to cross the Fermi level close to the Brillouin zone centre in Fig. 3b. We attribute all of these differences to the presence of two distinct types of Se-terminated surface in $AgCrSe_2$ (see Supplementary Fig. 5). For the low-temperature crystal structure shown in Fig. 1a, b, the Ag atoms sit directly atop Se sites (we denote this Se1) in the layer below, while sitting at the centre of a triangle of three Se sites (Se2) in the layer above. The Se1-Ag bond length is shorter than the Se2-Ag one[8], leading to a more covalent bond. Consequently, an imbalance can be expected in the charge transfer from Ag to different Se sites, with a slightly higher charge transfer from Ag to Se2 than to Se1 (Fig. 1b and Supplementary Fig. 6). The exact degree of hole doping at the $CrSe_2$-terminated surface will thus depend on whether the Se1 or Se2 layer is located in the surface plane, with increased surface hole doping expected for the latter (see also Supplementary Fig. 6). The variations in surface structure for Se1 and Se2 layers also provide a natural explanation for the change in transition matrix elements observed in our measurements in Fig. 3a, b, which would not be expected from a simple doping due to extrinsic e.g., defect-mediated mechanisms. This again suggests that the change in the Fermi level position observed here is related to the presence of Se1 and Se2 terminated surfaces in our studied samples.

Similar changes in k_F to those observed experimentally are found in our DFT calculations performed for the Se1 (Fig. 3c) and Se2 (Fig. 3d) surfaces, validating the above discussions. Intriguingly, we further find a significant, and termination-dependent, influence of spin-orbit coupling on the calculated electronic dispersion relations. In fact, inclusion of SOC in the calculations shown in Fig. 3 leads to an apparent splitting of the states *cf.* the calculations shown in Fig. 2 where SOC is neglected (cf.

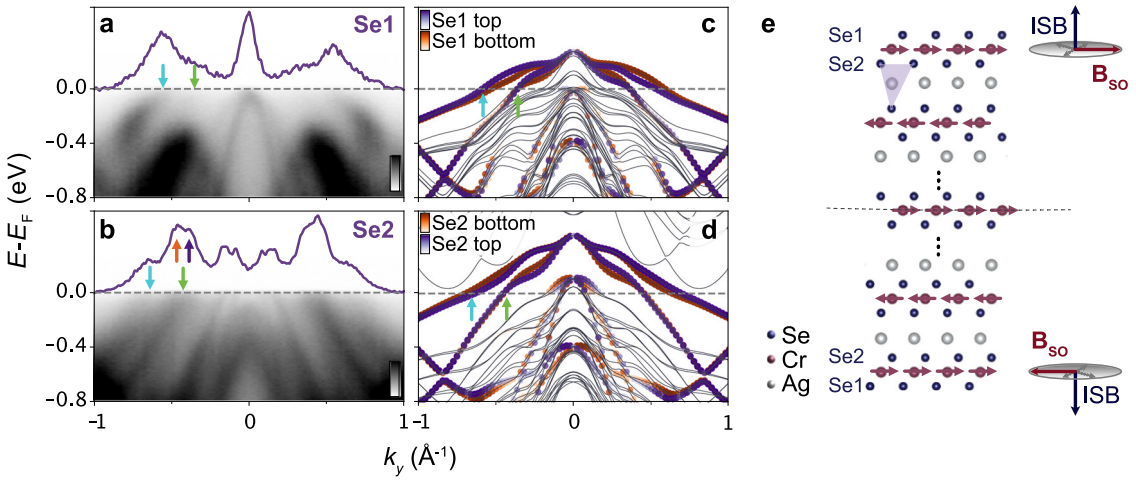

Fig. 3 Inversion symmetry breaking and spin-orbit coupling. ARPES measurements (sum of spectra measured using LH and LV polarised light, $h\nu = 69$ eV at $T \approx 18$ K) for **a** Se1 and **b** Se2 surface layers (see Fig. 1b). The green and blue arrows indicate how the two bands crossing the Fermi level are shifted to higher momenta for Se2 vs. Se1 surface terminations. The purple lines show MDCs extracted at the Fermi level, with evidence of an additional band splitting (purple and orange arrows). All of these features are in good agreement with our DFT calculations shown in **c**, **d**, which are projected onto the top (purple) and bottom (orange) surfaces of inversion-symmetric slab calculations. Spin-orbit coupling is included in these calculations. **e** Schematic of the supercell used for the DFT calculations for a Se1-terminated surface. The Cr magnetic moment is indicated by the arrows. The change in the direction of the inversion symmetry breaking (ISB) for the top and bottom surfaces will result in a switching of the effective spin-orbit field ($\mathbf{B}_{so}$). Rashba-type splitting resulting from this leads to the energetic splitting of the states at the top and bottom surfaces evident in **c**, **d**.

supplementary Fig. 7 for a direct comparison of the calculations with and without SOC). At first glance, this appears challenging to reconcile with the spin-polarised nature of the near-E_F states discussed above. However, by projecting our calculations onto the top and bottom surface of the supercell in Fig. 3c, d, it is clear that the observed splitting in fact results from a loss of degeneracy of states on the two opposite surfaces of the supercell.

DISCUSSION

Our calculations are performed using globally centrosymmetric supercells, as shown in Fig. 3e, with the lower half of the cell related to the upper half by an inversion (see Methods). Thus, both surfaces of the supercell are terminated by Se1 layers for the calculations shown in Fig. 3c, e and by Se2 layers in Fig. 3d. Furthermore, the two surfaces have the same magnetic moment orientation in the global co-ordinate system (Fig. 3e). Crucially, however, the surface contributes to the inversion symmetry breaking in this system, acting with opposite signs in the global co-ordinate system for the top and bottom surfaces. When combined with SOC, such inversion symmetry breaking can generically give rise to a Rashba-type interaction, described by a momentum-dependent spin-orbit field $\mathbf{B}_{so}$. In the sister compound $PtCoO_2$, the energy scale associated with the surface inversion symmetry breaking was found to be pronounced, leading to Rashba-type spin splittings on the CoO_2-terminated surface which reach as high as 60 meV[16], the full magnitude of the atomic spin-orbit coupling of Co 3*d* orbitals.

Here, the same edge-sharing octahedral configuration of the surface layer should unlock a similarly large energy scale for the surface inversion symmetry breaking. Furthermore, a comparable (albeit slightly weaker) SOC strength can be expected for the Cr *d*-orbitals, with additional mixing of Se character into these states (see Supplementary Fig. 8 for projection of Cr and Se weights) further enhancing the effective SOC strength. Yet, the underlying states crossing the Fermi level are already spin polarised due to the magnetic order (Fig. 2c), and the spin-orbit field can not therefore simply lift the spin degeneracy of the surface states as it would for a conventional Rashba effect in a spin-degenerate electron or hole gas[27–29].

Instead, it can be expected to perturb the energies of the spin-polarised states, with a form factor which acts oppositely at opposite momentum. Exactly this behaviour can be observed in Fig. 3c, d, where the states localised on opposite surfaces become split-off in energy, with a splitting that reverses at negative vs. positive momentum, and vanishes at the time-reversal symmetric Γ-point (see Supplementary Fig. 9 for a magnified view of this). This is entirely consistent with a Rashba-type spin-orbit interaction, acting with opposite signs for the opposite surfaces. Of course, in an ARPES experiment, only the top crystal surface is probed. From an experimental point of view, however, a similar effect can be expected for two different magnetic domains, with opposite spin orientation relative to the inversion symmetry breaking potential. Probing over such domains would mimic the effect of averaging over the top and bottom surfaces in our supercell calculations, leading to a splitting of the measured dispersions. In fact, for the Se2-terminated surface we observe weak signatures of such a band splitting, as evident in the asymmetric peak structure of the extracted momentum distribution curve at the Fermi level (see orange and purple arrows shown in Fig. 3b). We thus consider that the splitting here likely arises due to the presence of magnetic domains within our probing light spot.

Intriguingly, the projections onto the top and bottom surfaces in our calculations show opposite behaviour for the Se1 and Se2 surfaces. For example, along the Γ-K direction (positive k_y values in Fig. 3), the upper branches of the spin-orbit split states crossing the Fermi level are located on the bottom surface of the supercell for Se1, while they are located on the top surface for the Se2-terminated supercell. The states localised on opposite surfaces also exhibit a smaller energetic splitting for the Se2 vs. the Se1-terminated supercells. We attribute this to a delicate interplay between the surface inversion symmetry breaking discussed above, and the inversion symmetry breaking that is present throughout the bulk crystal structure in the low-temperature R3*m* phase. For the Se1-terminated surface, the effective dipole arising from the bulk inversion asymmetry contributes with the same sign as the inversion symmetry breaking at the surface, amplifying the effect and leading to spin splittings as large as 50 meV between the top- and bottom-layer

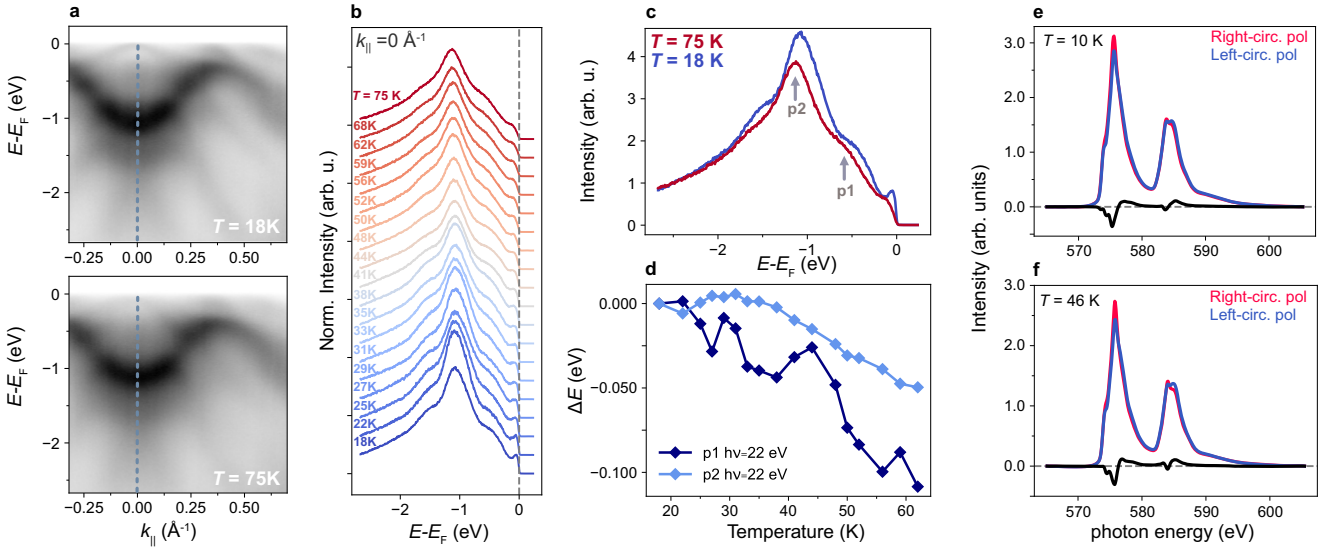

Fig. 4 Temperature dependent ARPES and XMCD measurements. a Example ARPES spectra at temperatures below ($T = 18$ K, top) and above ($T = 75$ K, bottom) T_N, measured using a photon energy of 22 eV and LH polarised light. **b** Temperature evolution of the energy distribution curve (EDC) extracted at the Γ-point (dashed lines in **a**). **c** Comparison of the high and low-temperature EDCs showing clear additional broadening at high temperatures, as well as peak shifts to higher binding energy. **d** Extracted energy shift of peaks p1 and p2 from fits to such EDCs as a function of temperature. **e**, **f** X-ray absorption spectra across the Cr $L_{2,3}$ edge with left- (blue curve) and right- (red curve) circularly polarised light, measured in an applied magnetic field of 1.4 T, together with the associated XMCD signal (black curve). These spectra were also measured **e** below (10 K) and **f** above (46 K) the magnetic transition.

surface bands in our calculations (Fig. 3c). For the Se2-terminated surface, the bulk and surface inversion symmetry breaking now effectively oppose each other, leading to an inversion in the energetic splitting of the top and bottom layer states as compared to that of the Se1 termination.

Together, these results point to significant Rashba-type interactions resulting from both the bulk and surface inversion asymmetry in $AgCrSe_2$, leading to energy scales which are significant as compared to the magnetic interactions in this system. Interestingly, the Rashba-type coupling occurs for an itinerant electron gas at the surface, but one whose magnetism stems from the magnetic ordering in the bulk which is best described as a local-moment system[13]. In order to gain more information about the nature of the surface magnetic ordering, we show in Fig. 4 temperature-dependent ARPES measurements. Comparison of spectra measured at temperatures above and below the bulk magnetic ordering temperature of 32 K (Fig. 4a) do not show any dramatic differences for either the bulk or surface states. This points to a local-moment picture of the magnetism also in the vicinity of the surface layer, where the loss of long-range magnetic order occurs via fluctuations with a well-defined local-moment persisting above T_N. Consistent with this picture, our systematic temperature-dependent measurements through the bulk T_N (see also Supplementary Fig. 10 for comparison bulk magnetisation data) show only small changes in the measured peak positions (Fig. 4b–d) with increasing temperature. Notably, no Stoner collapse of the exchange splitting in the electronic band structure is observed, as might have been typically expected for an itinerant magnet.

To further validate the localised nature of the magnetic order here, we show in Fig. 4e, f X-ray magnetic circular dichroism measurements (XMCD) below and above the bulk T_N, respectively. These are performed in total electron yield mode under an applied magnetic field of 1.4 T, to provide an element-specific and surface-sensitive magnetic probe. Low-temperature spectra (Fig. 4e), give rise to a clear magnetic circular dichroism, confirming the presence of magnetic order in the near-surface region of the sample, and a lack of any surface magnetic dead layer. Crucially, measurements above T_N (Fig. 4f) still yield a pronounced circular dichroism in this applied field. This reflects the paramagnetic nature of the samples, with well-defined local moments remaining above T_N, that are readily polarised by the applied field. This leads to an interesting situation where, despite the electron gas being itinerant at the surface, the magnetic character is predominantly derived from local-moment interactions, as observed in the bulk. As discussed above, it further exhibits a marked influence of SOC, which can be expected to give rise to non-trivial magnetic states and textures at the surface. This motivates future studies by, for example, spin-polarised scanning tunnelling microscopy and spin-resolved ARPES.

Indeed, our study establishes the surface of $AgCrSe_2$ as a particularly rich environment for investigating the spin-polarised surface hole gas which naturally arises via its intrinsic electronic reconstruction. It points to the pronounced influence of spin-orbit coupling on the surface electronic states of delafossite-type materials, and opens different avenues for exploring their interplay with magnetic order, where complex magnetic textures can be expected to result[30,31]. Excitingly, given the semiconducting bulk of $AgCrSe_2$, it may further be possible to tune the degree of surface inversion symmetry breaking, and the relative importance of surface and bulk inversion asymmetry, via the field-effect or at interfaces with ferroelectric compounds[32]. Achieving this type of control would provide a proof of principle for gaining electrical control of spintronic functionality in materials hosting similar spin-polarised surface electron gases.

METHODS

ARPES

Single crystal samples of $AgCrSe_2$ were grown via a chemical transport reaction using chlorine as a transport agent, as described in detail in Ref. [13]. All samples were top-posted and cleaved in situ at a base pressure lower than 10^{-10} mbar. Angle-resolved photoemission experiments (ARPES) and soft x-ray XPS measurements in a spatial mapping mode (Fig. 1) were carried out at the nano-ARPES branch of the I05 endstation at Diamond Light

Source, UK, using a capillary optic with a spot size of ~ 4 µm. All mapping data was acquired at a base temperature of ~ 35 K and measured with a Scienta Omicron DA30 analyzer. The measurements of the Fermi surface in Fig. 2e were obtained at the high-resolution branch of the I05 endstation at Diamond Light Source, with a measurement temperature of ~ 8 K. The endstation is equipped with an MB Scientific analyzer, and the spot size on the sample is *ca.* 50 µm. All other high-resolution ARPES data presented in Figs. 2 and 3 were obtained from experiments at the Bloch beamline at MAX-IV synchrotron Lund, Sweden, using a Scienta Omicron DA30-L analyzer and a spot size of ≈ 10 × 15 µm, at a base temperature of ≈ 18 K. For the k_z dependent measurements, the photon energy was tuned between 20 and 140 eV, and analysed within a standard free-electron final state model assuming an inner potential of $V_0 = 12$ eV.

XMCD

X-ray absorption spectroscopy (XAS) and X-ray magnetic circular dichroism (XMCD) measurements were performed at the I10 beamline at Diamond Light Source, UK, using the electromagnet end-station. Samples were top-posted and cleaved in situ at a base pressure lower than 10^{-9} mbar. All measurements were carried out in total electron yield (TEY) mode over an energy range spanning the Cr $L_{2,3}$ edge ($2p \rightarrow 3d$) with a probing depth of $\approx 3-5$ nm. To probe the in-plane magnetic moment a grazing incidence angle of 70° (with 0° being normal to the surface) was used. All measurements were performed with an applied field of 1.4 T using 100% left- and right-circularly polarised light above (46 K) and below (10 K) the magnetic transition temperature.

DFT

Electronic structures were calculated using a local-orbital minimum basis method implemented in the full-potential FPLO code, version fplo18.00-52 (http://www.fplo.de)[33,34]. The calculations were based on the localised density approximation (LDA) with Perdew-Wang-92 exchange-correlation functional[35]. We assumed antiferromagnetic (AFM) ordering where the Cr magnetic moments are aligned ferromagnetically in the *ab* plane with an easy axis along the crystalline *b*-axis, and with anti-parallel coupling between the layers. The spin-orbit coupling effect was treated non-perturbatively by solving the full Kohn-Sham-Dirac equation[36] in a single-step calculation. The Brillouin zone was sampled with a *k*-mesh of 1024 *k*-points (16 × 16 × 4 mesh, 282 points in the irreducible wedge of the Brillouin zone). For surface electronic structures we constructed periodic arrangements of Ag and Se terminated slab structures including nine Cr layers, using the bulk crystal structure of $AgCrSe_2$ with a thick vacuum of 16 Å between adjacent slabs. The bulk structure in the rhombohedral space group *R*3*m* was used, with the experimental lattice parameters of $a = b = 3.6798$ Å, $c = 21.225$ Å at room temperature[8]. To facilitate the convergence of self-consistent calculations, we formed centrosymmetric cells by applying a combination of C_2 rotation and mirror symmetry about the central Cr layer of the supercell (see, e.g., Fig. 3e). We then constructed two distinct slab structures, one with Se1 and the other with Se2 atoms in the central $CrSe_2$ block, in order to compare the effects of the Se1 and Se2 surface terminations.

DATA AVAILABILITY

The research data supporting this publication can be accessed at https://doi.org/10.17630/1c274296-4250-4540-af59-b7f961819101[37].

Received: 21 June 2023; Accepted: 9 October 2023;
Published online: 21 October 2023

REFERENCES

1. Gascoin, F. & Maignan, A. Order–disorder transition in $AgCrSe_2$: a new route to efficient thermoelectrics. *Chem. Mater.* **23**, 2510–2513 (2011).
2. Wu, D. et al. Revisiting $AgCrSe_2$ as a promising thermoelectric material. *Phys. Chem. Chem. Phys.* **18**, 23872–23878 (2016).
3. Li, B. et al. Liquid-like thermal conduction in intercalated layered crystalline solids. *Nat. Mater.* **17**, 226–230 (2018).
4. Damay, F. et al. Localised Ag+ vibrations at the origin of ultralow thermal conductivity in layered thermoelectric $AgCrSe_2$. *Sci. Rep.* **6**, 23415 (2016).
5. Xie, L., Feng, J. H., Li, R. & He, J. Q. First-principles study of anharmonic lattice dynamics in low thermal conductivity $AgCrSe_2$: evidence for a large resonant four-phonon scattering. *Phys. Rev. Lett.* **125**, 245901 (2020).
6. Mackenzie, A. P. The properties of ultrapure delafossite metals. *Rep. Prog. Phys.* **80**, 032501 (2017).
7. Marquardt, M. A., Ashmore, N. A. & Cann, D. P. Crystal chemistry and electrical properties of the delafossite structure. *Thin Solid Films* **496**, 146–156 (2006).
8. Van Der Lee, A. & Wiegers, G. A. Anharmonic thermal motion of Ag in $AgCrSe_2$: a high-temperature single-crystal X-Ray diffraction study. *J. Solid State Chem.* **82**, 216–224 (1989).
9. Ding, J. et al. Anharmonic lattice dynamics and superionic transition in $AgCrSe_2$. *Proc. Natl Acad. Sci. USA* **117**, 3930–3937 (2020).
10. Murphy, D. W., Chen, H. S. & Tell, B. Superionic Conduction in $AgCrS_2$ and $AgCrSe_2$. *J. Electrochem. Soc.* **124**, 1268 (1977).
11. Bongers, P. et al. Structures and magnetic properties of some metal (I) chromium (III) sulfides and selenides. *J. Phys. Chem. Solids* **29**, 977–984 (1968).
12. Gautam, U. K., Seshadri, R., Vasudevan, S. & Maignan, A. Magnetic and transport properties, and electronic structure of the layered chalcogenide $AgCrSe_2$. *Solid State Commun.* **122**, 607–612 (2002).
13. Baenitz, M. et al. Planar triangular S=3/2 magnet $AgCrSe_2$: magnetic frustration, short range correlations, and field-tuned anisotropic cycloidal magnetic order. *Phys. Rev. B* **104**, 134410 (2021).
14. Engelsman, F. M. R., Wiegers, G. A. & Jellinek, F. Crystal structures and magnetic structures of some metal(I) Chromium (III) sulfides and selenides. *J. Solid State Chem.* **6**, 574 (1973).
15. Yano, R. & Sasagawa, T. Crystal growth and intrinsic properties of $ACrX_2$ (A = Cu, Ag; X = S, Se) without a secondary phase. *Cryst. Growth Des.* **16**, 5618–5623 (2016).
16. Sunko, V. et al. Maximal Rashba-like spin splitting via kinetic-energy-coupled inversion-symmetry breaking. *Nature* **549**, 492–496 (2017).
17. Mazzola, F. et al. Itinerant ferromagnetism of the Pd-terminated polar surface of $PdCoO_2$. *Proc. Natl Acad. Sci. USA* **115**, 12956–12960 (2018).
18. Eastman, D. E., Himpsel, F. J. & van der Veen, J. F. Photoemission studies of surface core-level shifts and their applications. *J. Vac. Sci. Technol.* **20**, 609–616 (1982).
19. Edwards, B. et al. Giant valley-Zeeman coupling in the surface layer of an intercalated transition metal dichalcogenide. *Nat. Mater.* **22**, 459–465 (2023).
20. Takahashi, H. et al. Spin-orbit-derived giant magnetoresistance in a layered magnetic semiconductor $AgCrSe_2$. *Phys. Rev. Mater.* **6**, 054602 (2022).
21. Hua, Y. et al. Tuning the electric transport behavior of $AgCrSe_2$ by intrinsic defects. *Sci. China Chem.* **64**, 1970–1975 (2021).
22. Shiomi, Y., Akiba, T., Takahashi, H. & Ishiwata, S. Giant piezoelectric response in superionic polar semiconductor. *Adv. Electron. Mater.* **4**, 1800174 (2018).
23. Nakagawa, N., Hwang, H. Y. & Muller, D. A. Why some interfaces cannot be sharp. *Nat. Mater.* **5**, 204–209 (2006).
24. Hwang, H. Y. et al. Emergent phenomena at oxide interfaces. *Nat. Mater.* **11**, 103–113 (2012).
25. Kim, K., Choi, H. C. & Min, B. I. Fermi surface and surface electronic structure of delafossite $PdCoO_2$. *Phys. Rev. B* **80**, 035116 (2009).
26. Mazzola, F. et al. Tuneable electron–magnon coupling of ferromagnetic surface states in $PdCoO_2$. *npj Quantum Mater.* **7**, 20 (2022).
27. Bychkov, Yu. A. & Rashba, É. I. Properties of a 2D electron gas with lifted spectral degeneracy. *Sov. J. Exp. Theor. Phys. Lett.* **39**, 78 (1984).
28. LaShell, S., McDougall, B. A. & Jensen, E. Spin splitting of an Au(111) surface state band observed with angle resolved photoelectron spectroscopy. *Phys. Rev. Lett.* **77**, 3419–3422 (1996).
29. King, P. D. C. et al. Large tunable Rashba spin splitting of a two-dimensional electron gas in Bi_2Se_3. *Phys. Rev. Lett.* **107**, 096802 (2011).
30. Park, K. et al. Nonreciprocal directional dichroism at telecom wavelengths. *npj Quantum Mater.* **7**, 38 (2022).
31. Butykai, Á. et al. Squeezing the periodicity of Néel-type magnetic modulations by enhanced Dzyaloshinskii-Moriya interaction of 4d electrons. *npj Quantum Mater.* **7**, 26 (2022).
32. Huyan, H. et al. Direct observation of polarization-induced two-dimensional electron/hole gases at ferroelectric-insulator interface. *npj Quantum Mater.* **6**, 88 (2021).

33. Koepernik, K. & Eschrig, H. Full-potential nonorthogonal local-orbital minimum-basis band-structure scheme. *Phys. Rev. B* **59**, 1743–1757 (1999).
34. Opahle, I., Koepernik, K. & Eschrig, H. Full-potential band-structure calculation of iron pyrite. *Phys. Rev. B* **60**, 14035–14041 (1999).
35. Perdew, J. P. & Wang, Y. Accurate and simple analytic representation of the electron-gas correlation energy. *Phys. Rev. B* **45**, 13244–13249 (1992).
36. Eschrig, H., Richter, M. & Opahle, I. Chapter 12 - relativistic solid state calculations. In Schwerdtfeger, P. (ed.) *Relativistic Electronic Structure Theory*, vol. 14 of *Theoretical and Computational Chemistry*, 723–776, (Elsevier, 2004).
37. Siemann, G.-R. et al. Spin-orbit coupled spin-polarised hole gas at the $CrSe_2$-terminated surface of $AgCrSe_2$ (dataset). Dataset. University of St Andrews Research Portal, https://doi.org/10.17630/1c274296-4250-4540-af59-b7f961819101 (2023).

ACKNOWLEDGEMENTS

We thank Tommaso Antonelli for useful discussions and are grateful to Ulrike Nitzsche for technical support at the IFW high-performance computational environment. We gratefully acknowledge support from the European Research Council (through the QUESTDO project, 714193), the Engineering and Physical Sciences Research Council (Grant No. EP/T02108X/1), and the Leverhulme Trust (Grant No. RL-2016-006). S.-J.K., E.A.M., A.Z., and I.M. gratefully acknowledge studentship support from the International Max-Planck Research School for Chemistry and Physics of Quantum Materials. We gratefully acknowledge MAX IV Laboratory for time on the Bloch beamline under Proposal Nos. 20190302, 20190735, 20200227, and Diamond Light Source for access to Beamlines I05 and I10 (Proposals SI28412, SI31035, and MM28727), which contributed to the results presented here. Research conducted at MAX IV, a Swedish national user facility, is supported by the Swedish Research Council under contract 2018-07152, the Swedish Governmental Agency for Innovation Systems under contract 2018-04969, and Formas under contract 2019-02496. The research leading to this result has been supported by the project CALIPSOplus under Grant Agreement 730872 from the EU Framework Programme for Research and Innovation HORIZON 2020. For the purpose of open access, the authors have applied a Creative Commons Attribution (CC BY) licence to any Author Accepted Manuscript version arising.

AUTHOR CONTRIBUTIONS

G.-R.S., E.A.M., P.A.E.M., A.Z., B.E., I.M., F.M., L.T., O.J.C., and P.D.C.K. measured the ARPES data, which was analysed by G.-R.S.; S.-J.K. and H.R. performed the DFT calculations; M.S., H.Z., and M.B. grew and characterised the samples; G.-R.S., B.A., C.B., T.H., and G.v.d.L. measured the XMCD data; M.D.W., T.K., P.B., C.M.P., M.L., H.F., K.A., and T.B. maintained the Diamond I05 and I10 and Max-IV Bloch beam lines and provided experimental support, including for remote synchrotron beamtimes; P.D.C.K. directed the project; G.-R.S., S.-J.K., H.R., and P.D.C.K. wrote the manuscript with contributions from all authors.

COMPETING INTERESTS

The authors declare no competing interests.

ADDITIONAL INFORMATION

Supplementary information The online version contains supplementary material available at https://doi.org/10.1038/s41535-023-00593-4.

Correspondence and requests for materials should be addressed to Phil D. C. King.

Reprints and permission information is available at http://www.nature.com/reprints

Publisher's note Springer Nature remains neutral with regard to jurisdictional claims in published maps and institutional affiliations.